Journal of Computational Physics 229 (2010) 6715–6731

Contents lists available at ScienceDirect

Journal of Computational Physics

journal homepage: www.elsevier.com/locate/jcp

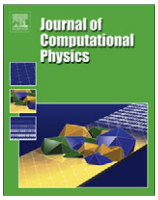

A high-order gas-kinetic Navier–Stokes flow solver

Qibing Li [a], Kun Xu [b,*], Song Fu [a]

[a] *Department of Engineering Mechanics, Tsinghua University, Beijing 100084, China*
[b] *Mathematics Department, Hong Kong University of Science and Technology, Hong Kong*

ARTICLE INFO

Article history:
Received 3 June 2009
Received in revised form 11 April 2010
Accepted 20 May 2010
Available online 31 May 2010

Keywords:
Navier–Stokes eqautions
Boltzmann equation
Gas-kinetic scheme
High-order method

ABSTRACT

The foundation for the development of modern compressible flow solver is based on the Riemann solution of the inviscid Euler equations. The high-order schemes are basically related to high-order spatial interpolation or reconstruction. In order to overcome the low-order wave interaction mechanism due to the Riemann solution, the temporal accuracy of the scheme can be improved through the Runge–Kutta method, where the dynamic deficiencies in the first-order Riemann solution is alleviated through the sub-step spatial reconstruction in the Runge–Kutta process. The close coupling between the spatial and temporal evolution in the original nonlinear governing equations seems weakened due to its spatial and temporal decoupling. Many recently developed high-order methods require a Navier–Stokes flux function under piece-wise discontinuous high-order initial reconstruction. However, the piece-wise discontinuous initial data and the hyperbolic-parabolic nature of the Navier–Stokes equations seem inconsistent mathematically, such as the divergence of the viscous and heat conducting terms due to initial discontinuity. In this paper, based on the Boltzmann equation, we are going to present a time-dependent flux function from a high-order discontinuous reconstruction. The theoretical basis for such an approach is due to the fact that the Boltzmann equation has no specific requirement on the smoothness of the initial data and the kinetic equation has the mechanism to construct a dissipative wave structure starting from an initially discontinuous flow condition on a time scale being larger than the particle collision time. The current high-order flux evaluation method is an extension of the second-order gas-kinetic BGK scheme for the Navier–Stokes equations (BGK-NS). The novelty for the easy extension from a second-order to a higher order is due to the simple particle transport and collision mechanism on the microscopic level. This paper will present a hierarchy to construct such a high-order method. The necessity to couple spatial and temporal evolution nonlinearly in the flux evaluation can be clearly observed through the numerical performance of the scheme for the viscous flow computations.

1. Introduction

The need for high-order numerical methods for the Navier–Stokes equations has been widely recognized in engineering applications, such as vortex-dominated flows, aeroacoustic noise predictions, LES/DNS computations for complex configurations. The current existing and popular high-order methods include the Essential Non-Oscillatory (ENO) [7], Weighted Essential Non-Oscillatory (WENO) [10], Discontinuous Galerkin (DG) [21,3], Spectral Difference (SD) [15], Spectral Volume (SV) methods [25], Arbitrary accuracy DERivative (ADER) Riemann problem [23], compact schemes [4,19], multi-moment

---

* Corresponding author.
E-mail addresses: lqb@tsinghua.edu.cn (Q. Li), makxu@ust.hk (K. Xu), fs-dem@tsinghua.edu.cn (S. Fu).

0021-9991/$ - see front matter © 2010 Elsevier Inc. All rights reserved.
doi:10.1016/j.jcp.2010.05.019

constrained finite volume (MCV) method [8], and many others. Among these high-order methods, DG, SV, and SD methods are similar in the way that they share the same solution space, i.e. the space of piece-wise discontinuous polynomials, and a first-order Riemann solution is used at the element interface to provide solution for information exchange across discontinuous elements and appropriate numerical dissipation necessary to achieve stability. For ADER method, the main part is still the first-order Riemann solution and approximate linear equations are solved for high-order terms. For the MCV method, higher-order (derivative) Riemann problems are solved numerically for the information exchange across cell boundaries. One benefit of this is that the MCV enjoys a larger allowable CFL time step for stability.

For high-order schemes, such as ENO, WENO, DG, SV, and SD methods, a high-order polynomial reconstruction (updated or interpolated) is obtained within each element or control volume. The physics of wave propagation starting from the high-order initial condition around the cell interface is accounted for through the Riemann solver, where two constant states are used for the flux evaluation [5,22]. Even with the high-order spatial reconstruction, the physical evolution process from the initial data is basically coming from a first-order physical mechanism. This is probably the main reason why for any high-order scheme the simulation results are sensitive to the limiters or reconstruction methods used. Therefore, many detectors, such as Harten's [6], Jameson's [9], and WENOs [10], have been invented to construct the point-wise values at the cell interfaces. In some flow problems, such as shock boundary layer interactions, the solution seems to be extremely sensitive to the detector used [19].

For the Navier–Stokes equations, the situation becomes even worse due to the hyperbolic-parabolic nature of the governing equations and the discontinuities in the reconstructed data. Certainly, the use of Runge–Kutta method helps for the improvement of time accuracy, but intrinsic nonlinear spatial and temporal coupling in the governing equations gets weakened. Physically, a solution should be one emerged directly from the discontinuous polynomials. If the whole curves on both sides of a discontinuity can be taken into account in the gas evolution process, the numerical solution will not be so sensitive to the point-wise values. So, in order to construct a high-order scheme, the development of a high-order NS flux function directly from a discontinuous high-order initial condition is important and preferable. Theoretically, the NS equations are coming from a model on the macroscopic scale and they require smooth flow distributions. But, due to the numerical side-effect, such as the cell resolution is not enough to resolve the physical structure, a discontinuity at the cell interface is artificially created. With the discontinuity initial condition, the Navier–Stokes formulations have severe difficulties mathematically due to the assumption of continuous function associated with the dissipative terms. A convenient remedy for this in the current CFD community is to detect the shock discontinuity in the initial reconstruction, then, one-sided finite differences to discretize the dissipative terms at the shock point are basically used. But, to get a reliable detector or limiter in multidimensional case is not an easy task.

Based on the gas-kinetic theory, the Navier–Stokes equations can be derived from the Boltzmann equation using the Chapman–Enskog expansion. Theoretically, a Navier–Stokes solver can be obtained by solving the Boltzmann equation, or a simplified kinetic collision model. However, the kinetic equation does not require any smoothness or continuity in its initial gas distribution. So, it naturally fits with the high-order piece-wise discontinuous initial data of a high-order reconstruction. The initial piece-wise discontinuity polynomials for the flow variables may be inconsistent with the underlying modeling of the Navier–Stokes equations, but they are perfectly acceptable by the Boltzmann equation.

In a gas-kinetic representation, all flow variables are moments of a single particle distribution function. Since a gas distribution function contains both equilibrium and non-equilibrium flow properties, the inviscid and viscous terms are obtained simultaneously. In the past years, a BGK-NS method based on the gas-kinetic BGK model [1] has been developed for the Navier–Stokes solutions under the linear polynomials for the mass, momentum, and energy distributions separated by a discontinuity at the origin [27]. The BGK-NS method has been successfully applied in many engineering applications, especially for the hypersonic viscous and heat conducting flows [29,12,13]. Later, an attempt to develop a higher-order gas-kinetic scheme has been made in the continuous initial reconstruction case [14]. This paper concerns with the construction of a third-order gas-kinetic flux function for the Navier–Stokes equations under piece-wise discontinuous initial condition. Instead of initial piece-wise linear distributions, two smooth parabolic curves for the conservative variables separated with a discontinuity at the origin are used as an initial condition. The generalization of the current methodology to arbitrary piece-wise smooth curves can be done accordingly. The possibility to construct such a method is mainly due to the simple particle transport mechanism in the microscopic level, i.e. free transport and collisions. The initial discontinuity jump and the ratio between time interval and particle collision time determine the emerging of wave patterns associated with the NS solutions. The high-order gas-kinetic scheme presented in this paper provides a valuable NS flux function, which can be implemented to many high-order computational fluid dynamic methods.

The paper is arranged in the following. Section 2 is about the construction of the third-order gas-kinetic Navier–Stokes flux function under piece-wise discontinuous parabolic flow distributions. Section 3 is the analysis of the scheme and introduces its possible generalization to develop a multidimensional scheme. Section 4 is the numerical examples which illustrate the importance to develop a high-order flux function. Last section is the conclusion.

2. A high-order gas-kinetic Navier–Stokes flow solver

The focus of this section is to present a Navier–Stokes flux function under the generalized initial data by solving the gas-kinetic BGK equation. The developed scheme is called High-order BGK (HBGK) scheme. A two-dimensional formulation will be presented.

2.1. High-order initial data reconstruction

Any high-order initial reconstruction, such as ENO, WENO, or DG methods can be used to obtain the subcell polynomials for the mass, momentum and energy distributions. For the conservative flow variables,

$$W = (\rho, \rho U, \rho V, \rho E)^T$$

in the x-direction the reconstructed data are

$$W(x,0) = \begin{cases} W_L + \left(\frac{\partial W_L}{\partial x}\right)x + \frac{1}{2}\left(\frac{\partial^2 W_L}{\partial x^2}\right)x^2, & x < 0, \\ W_R + \left(\frac{\partial W_R}{\partial x}\right)x + \frac{1}{2}\left(\frac{\partial^2 W_R}{\partial x^2}\right)x^2, & x \geqslant 0, \end{cases} \tag{1}$$

where $x = 0$ is the cell interface. The focus of this paper is to construct a time-dependent flux function underlying the above initial condition. The reconstruction method used in this paper is the parameter-free generalized moment (PFGM) limiter method [30]. Inside each cell i, the conservative variables are reconstructed as

$$W_i(x) = \overline{W}_i^{(0)} + \overline{W}_i^{(1)}(x - x_i) + \frac{1}{2}\overline{W}_i^{(2)}\left[(x - x_i)^2 - \frac{1}{12}h^2\right], \tag{2}$$

where h is the cell size and the coefficients

$$\overline{W}_i^{(0)} = \overline{W}_i,$$
$$\overline{W}_i^{(1)} = (\overline{W}_{i+1} - \overline{W}_{i-1})/2h,$$

and

$$\overline{W}_i^{(2)} = (\overline{W}_{i+1} - 2\overline{W}_i + \overline{W}_{i-1})/h^2$$

with cell averaged conservatives variables $\overline{W}_{i-1}, \overline{W}_i$ and $\overline{W}_{i+1}$ in $(i-1)$th, ith and $(i+1)$th cells. The above cell-averaged derivatives are limited in a hierarchical manner using a minmod-type limiter. Starting from the highest order derivatives, $\overline{W}_i^{(p)}$ is limited using

$$\overline{Y}_i^{(p)} = \min\mathrm{mod}\left(\overline{W}_i^{(p)}, 1.5\frac{\overline{W}_{i+1}^{(p-1)} - \overline{W}_i^{(p-1)}}{h}, 1.5\frac{\overline{W}_i^{(p-1)} - \overline{W}_{i-1}^{(p-1)}}{h}\right). \tag{3}$$

If $\overline{Y}_i^{(p)} = \overline{W}_i^{(p)}$, the highest derivative is not altered. No further limiting is required, and the solution remains the same. Otherwise, the limiting process proceeds to the next lower derivative in a similar fashion. Finally, the limited polynomial inside each cell is written

$$W_i(x) = \overline{Y}_i^{(0)} + \overline{Y}_i^{(1)}(x - x_i) + \frac{1}{2}\overline{Y}_i^{(2)}\left[(x - x_i)^2 - \frac{1}{12}h^2\right], \tag{4}$$

which is the basic reconstruction used in this paper. The above reconstruction, i.e. $\overline{W}^{(p)}$, is based on standard central-difference methods, which are applied to all conservative variables in this paper. The order of the reconstruction is defined by the highest derivatives included, i.e. $p = 3$ means third-order reconstruction and $p = 2$ is the second-order one. The reconstruction of the polynomial is basically independent from the order of the flux evaluation scheme. For example, the time-dependent flux in the second-order BGK-NS scheme [27] is based on the evolution of linearly distributed mass, momentum and energy. But, a high-order reconstruction method can be still used to get the linear slopes, such as BGK-NS method with $p = 3$ reconstruction.

Even though the initial reconstruction is critically important for any high-order method, the focus of this paper is on the flux evaluation. We cannot make sure that the above reconstruction scheme is optimal. The use of this reconstruction is solely due to its simplicity. To use other reconstruction scheme will also be investigated in future.

2.2. Gas-kinetic BGK model

The two-dimensional BGK equation can be written as [1,24]

$$f_t + uf_x + vf_y = \frac{g - f}{\tau},$$

where f is the gas distribution function and g is the equilibrium state approached by f. Both f and g are functions of space (x,y), time t, particle velocities (u, v), and internal variable ξ. The particle collision time τ is related to the viscosity and heat conduction coefficients. A directional splitting scheme will be developed in this paper. For a 2D flow, such as in the x-direction, the kinetic equation becomes,

$$f_t + uf_x = \frac{g-f}{\tau}. \tag{5}$$

The equilibrium state is a Maxwellian distribution,

$$g = \rho\left(\frac{\lambda}{\pi}\right)^{\frac{K+2}{2}} e^{-\lambda((u-U)^2+(v-V)^2+\xi^2)},$$

where ρ is the density, (U,V) is the macroscopic velocity in the x and y directions, and λ is equal to $m/2kT$, m is the molecular mass, k is the Boltzmann constant, and T is the temperature. For a 2D flow, the total number of degrees of freedom K in ξ is equal to $(3-\gamma)/(\gamma-1)-1$ [27]. For example, for a diatomic gas with $\gamma = 7/5$, K is equal to 3 to account for the particle motion in the z-direction and two rotational degrees of freedom. In the equilibrium state, the internal variable $\xi^2$is equal to $\xi^2 = \xi_1^2 + \xi_2^2 + \cdots + \xi_K^2$. The relation between mass ρ, momentum $(\rho U, \rho V)$, and energy ρE densities with the distribution function f is

$$\begin{pmatrix} \rho \\ \rho U \\ \rho V \\ \rho E \end{pmatrix} = \int \psi_\alpha f d\Xi, \quad \alpha = 1,2,3,4, \tag{6}$$

where ψ_α is the component of the vector of moments

$$\boldsymbol{\psi} = (\psi_1, \psi_2, \psi_3, \psi_4)^T = \left(1, u, v, \frac{1}{2}(u^2 + v^2 + \xi^2)\right)^T,$$

and $d\Xi = dudvd\xi_1 d\xi_2 \cdots d\xi_K$ is the volume element in the phase space with $d\xi = d\xi_1 d\xi_2 \cdots d\xi_K$. Since mass, momentum, and energy are conserved during particle collisions, f and g satisfy the conservation constraint,

$$\int (g-f)\psi_\alpha d\Xi = 0, \quad \alpha = 1,2,3,4, \tag{7}$$

at any point in space and time.

Based on the above BGK equation, in order to derive the Navier–Stokes equations, the Chapman–Enskog expansion is used. The expansion requires the continuity and smoothness of the macroscopic flow variables. However, for the kinetic equation (5) itself, this requirement is not necessary. Under the initial piece-wise discontinuous polynomial, the kinetic equation covers a wider applicable regime than the Navier–Stokes equations. Different from the previous BGK-NS flow solver based on the linear polynomial expansion of the conservative variables on both sides of a cell interface [27], this paper will target on the numerical NS solutions under a parabolic polynomial expansions (1). To extend the current method further to use even higher order polynomials is straightforward.

2.3. High-order BGK flow solver

The general solution f of the BGK model (5) at a cell interface $x_{j+1/2}$ and time t is

$$f(x_{j+1/2}, t, u, v, \xi) = \frac{1}{\tau}\int_0^t g(x', t', u, v, \xi) e^{-(t-t')/\tau} dt' + e^{-t/\tau} f_0(x_{j+1/2} - ut), \tag{8}$$

where $x' = x_{j+1/2} - u(t-t')$ is the particle trajectory and f_0 is the initial gas distribution function f at the beginning of each time step ($t = 0$). Two unknowns g and f_0 must be specified in Eq. (8) in order to obtain the solution f. In order to simplify the notation, $x_{j+1/2} = 0$ will be used in the following text.

In previous BGK-NS scheme [27,12], based on the initial macroscopic variables, the initial gas distribution function f_0 is constructed as

$$f_0 = \begin{cases} g^l\left[1 + a^l x - \tau(a^l u + A^l)\right], & x < 0, \\ g^r\left[1 + a^r x - \tau(a^r u + A^r)\right], & x \geqslant 0, \end{cases} \tag{9}$$

where g^l and g^r are the Maxwellian distributions at the left and right hand sides of the cell interface, a and A are associated with its spatial and temporal derivatives of an equilibrium state. The non-equilibrium parts satisfy the compatibility condition,

$$\begin{aligned} &\int (a^l u + A^l)\psi g^l d\Xi = 0, \\ &\int (a^r u + A^r)\psi g^r d\Xi = 0. \end{aligned} \tag{10}$$

In the previous high-order DG-BGK schemes, even with high-order reconstruction, only linear slopes consistent with the above formulation are kept in the flux evaluation [16,17], and the Runge–Kutta methods are used for the time accuracy. Although the previous high-order kinetic method has a consistent third-order accuracy to certain standard test cases, the scheme is not a fully nonlinear method coupling spatial and temporal evolution from a high-order discontinuous polynomials.

In this paper, we are going to design a high-order BGK (HBGK) scheme which presents a time-dependent flux function directly from a discontinuous parabolic macroscopic flow distributions. For this HBGK scheme, the initial reconstruction of the conservative variables include second-order derivatives. First, based on the high-order polynomial reconstruction presented in Section 2.1, we need to evaluate the corresponding Chapman–Enskog distribution function for the Navier–Stokes equations on both sides of a cell interface. The Chapman–Enskog expansion of the kinetic equation to the Navier–Stokes order gives,

$$f_{NS}(x,t) = g(1 - \tau(au + A)),$$

where g is the equilibrium state,

$$a = (\partial g/\partial x)/g = a_1 + a_2 u + a_3 v + a_4(u^2 + v^2 + \xi^2)$$

and

$$A = (\partial g/\partial t)/g = A_1 + A_2 u + A_3 v + A_4(u^2 + v^2 + \xi^2),$$

where g, a, and A are functions of space and time. With a second-order initial polynomial distribution, a NS distribution function at time $t = 0$ can be constructed as

$$f_{NS}(x,0) = f_{NS}(0,0) + \frac{\partial f_{NS}}{\partial x}x + \frac{1}{2}\frac{\partial^2 f_{NS}}{\partial x^2}x^2 = g\left[1 - \tau(au + A) + ax - \tau(C + aA)x + (a^2 + b)\left(-\tau ux + \frac{1}{2}x^2\right)\right], \tag{11}$$

where $b = \partial a/\partial x$ and $C = \partial A/\partial x$. Therefore, with the initial discontinuous reconstruction (1), the corresponding NS non-equilibrium states on both sides of a cell interface can be constructed,

$$f_0 = \begin{cases} g^l\left[1 - \tau(a^l u + A^l) + a^l x - \tau(C^l + a^l A^l)x + ((a^l)^2 + b^l)(-\tau ux + \frac{1}{2}x^2)\right], & x < 0, \\ g^r\left[1 - \tau(a^r u + A^r) + a^r x - \tau(C^r + a^r A^r)x + ((a^r)^2 + b^r)(-\tau ux + \frac{1}{2}x^2)\right], & x \geqslant 0, \end{cases} \tag{12}$$

where all parameters are determined through the following relations, see Fig. 1. First, let us define the moments of the equilibrium states,

$$\langle \cdots \rangle_l = \int_{-\infty}^{\infty} g^l(\cdots)\psi\, d\Xi, \quad \langle \cdots \rangle_r = \int_{-\infty}^{\infty} g^r(\cdots)\psi\, d\Xi,$$

and

$$\langle \cdots \rangle_l|_{u>0} = \int_0^{\infty} g^l(\cdots)\psi\, d\Xi, \quad \langle \cdots \rangle_r|_{u<0} = \int_{-\infty}^{0} g^r(\cdots)\psi\, d\Xi.$$

The equilibrium states g^l and g^r are obtained from macroscopic point-wise values at the cell interface,

$$\int g^l \psi\, d\Xi = W_L, \quad \int g^r \psi\, d\Xi = W_R.$$

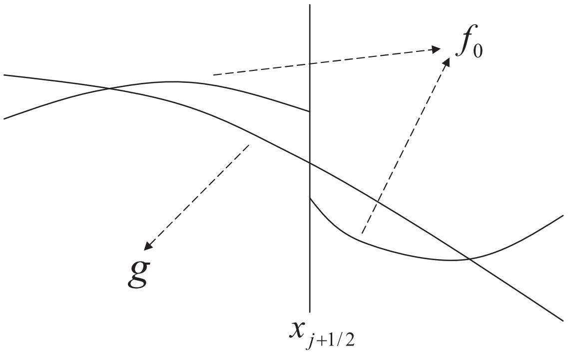

Fig. 1. Equilibrium and non-equilibrium gas distribution functions across a cell interface.

Then, parameters a and b in f_0 are determined using the slopes of macroscopic variables on the left and right hand sides of the cell interface separately,

$$\langle a^l\rangle_l = \partial W_L/\partial x, \quad \langle a^r\rangle_r = \partial W_R/\partial x,$$
$$\langle (a^l)^2 + b^l\rangle_l = \partial^2 W_L/\partial x^2, \quad \langle (a^r)^2 + b^r\rangle_r = \partial^2 W_R/\partial x^2.$$

Based on the compatibility condition (7), other parameters can be determined as

$$\langle A^l + a^l u\rangle_l = 0, \quad \langle A^r + a^r u\rangle_r = 0,$$
$$\langle C^l + a^l A^l + ((a^l)^2 + b^l)u\rangle_l = 0, \quad \langle C^r + a^r A^r + ((a^r)^2 + b^r)u\rangle_r = 0.$$

After having f_0, the equilibrium state g around ($x = 0$, $t = 0$) can be constructed with spatial and temporal accuracy consistent with f_0,

$$\begin{aligned} g(x,t) &= g_0 + \frac{\partial g_0}{\partial x}x + \frac{\partial g_0}{\partial t}t + \frac{1}{2}\frac{\partial^2 g_0}{\partial x^2}x^2 + \frac{1}{2}\frac{\partial^2 g_0}{\partial t^2}t^2 + \frac{\partial^2 g_0}{\partial x \partial t}xt \\ &= g_0\left[1 + ax + At + \frac{1}{2}(a^2+b)x^2 + \frac{1}{2}(A^2+B')t^2 + (C+aA)xt\right], \end{aligned} \tag{13}$$

where g_0, a, A, B', C will be determined later using the compatibility condition between f and g. Here, g_0 is a local Maxwellian distribution function located at the cell interface, see Fig. 1.

Let us first determine g_0 at ($x = 0$, $t = 0$), i.e.

$$g_0 = \rho_0\left(\frac{\lambda_0}{\pi}\right)^{\frac{K+2}{2}} e^{-\lambda_0((u-U_0)^2+(v-V_0)^2+\xi^2)}.$$

Taking the limit $t \to 0$ in Eq. (8) and substituting its solution into Eq. (7), the conservation constraint at ($x = 0$, $t = 0$) gives

$$\int g_0\psi\, d\Xi = W_0 = \int_{u>0}\int g^l\psi\, d\Xi + \int_{u<0}\int g^r\psi\, d\Xi, \tag{14}$$

where $W_0 = (\rho_0, \rho_0 U_0, \rho_0 V_0, \rho_0 E_0)^T$ is the macroscopic conservative flow variables located at the cell interface at time $t = 0$. Since g^l and g^r have been obtained earlier, the above moments can be evaluated explicitly. Therefore, the conservative variables ρ_0, $\rho_0 U_0$, $\rho_0 V_0$, and $\rho_0 E_0$ at the cell interface can be obtained, from which g_0 is uniquely determined. For example, λ_0 in g_0 can be found from

$$\lambda_0 = (K+2)\rho_0 \Bigg/ \left(4\left(\rho_0 E_0 - \frac{1}{2}\rho_0 U_0^2 - \frac{1}{2}\rho_0 V_0^2\right)\right).$$

Based on the above obtained conservative variables W_0 at the cell interface, and the cell averaged values $\overline{W}_j$ and $\overline{W}_{j+1}$ on the left and right hand sides of the cell interface, a unique continuous flow distribution can be fully determined,

$$W(x,0) = W_0 + \frac{\partial W_0}{\partial x}x + \frac{1}{2}\frac{\partial^2 W_0}{\partial x^2}x^2$$

from which the equilibrium gas distribution functions at time $t = 0$ in Eq. (13) can be obtained. With the definition

$$\langle \cdots \rangle = \int_{-\infty}^{\infty} g_0(\cdots)\psi\, d\Xi,$$

the corresponding terms in the distribution g in Eq. (13) can be obtained in the following,

$$\langle a\rangle = \frac{\partial W_0}{\partial x},$$

and

$$\langle b + a^2\rangle = \frac{\partial^2 W_0}{\partial x^2}.$$

Other parameters A, B', and C of $g(x,t)$ in Eq. (13) are determined by the compatibility conditions,

$$\langle A + au\rangle = 0,$$
$$\langle C + Aa + (a^2+b)u\rangle = 0,$$
$$\langle B' + A^2 + (C + Aa)u\rangle = 0.$$

Substitute Eq. (12) and (13) into Eq. (8), the gas distribution function f at a cell interface can be expressed as

$$\begin{aligned} f(x_{j+1/2},t,u,v,\xi) = {} & (1-e^{-t/\tau})g_0 + (-\tau+(\tau+t)e^{-t/\tau})aug_0 + (t-\tau+\tau e^{-t/\tau})Ag_0 + (2\tau^2-(t^2+2\tau t+2\tau^2)e^{-t/\tau}) \\ & \times(a^2+b)u^2g_0 + (t^2/2-\tau t+\tau^2-\tau^2e^{-t/\tau})(A^2+B')g_0 + (2\tau^2-\tau t-(2\tau^2+\tau t)e^{-t/\tau})(C \\ & + aA)ug_0 + e^{-t/\tau}(1-\tau(a^lu+A^l)-a^lut+\tau t(C^l+a^lA^l)u+\left(\tau t+\frac{1}{2}t^2\right)((a^l)^2+b^l)u^2)\mathrm{H}(u)g^l \\ & + e^{-t/\tau}(1-\tau(a^ru+A^r)-a^rut+\tau t(C^r+a^rA^r)u+\left(\tau t+\frac{1}{2}t^2\right)((a^r)^2+b^r)u^2)(1-\mathrm{H}(u))g^r. \end{aligned} \tag{15}$$

Then, the time-dependent numerical fluxes in the x-direction across the cell interface can be computed as

$$\begin{pmatrix} \mathcal{F}_\rho \\ \mathcal{F}_{\rho U} \\ \mathcal{F}_{\rho V} \\ \mathcal{F}_{\rho E} \end{pmatrix}_{j+1/2} = \int u \begin{pmatrix} 1 \\ u \\ v \\ \frac{1}{2}(u^2+v^2+\xi^2) \end{pmatrix} f(x_{j+1/2},t,u,v,\xi)d\Xi, \tag{16}$$

where $f(x_{j+1/2},t,u,v,\xi)$ is given in Eq. (15). By integrating the above equation in a whole time step $\Delta t = t^{n+1} - t^n$, we can get the total mass, momentum and energy transport across a cell interface within a time step. In other words, the current kinetic scheme fully couples the spatial and temporal evolution, no sub-steps or Runge–Kutta method are needed to get time accuracy of the scheme.

For the viscous and heat conducting flow computation, the BGK equation presents a unit Prandtl number. Numerically, since the heat flux can be explicitly evaluated at the cell interface, the above energy flux can be slightly modified in the current method to simulate flows with any Prandtl number [27].

2.4. Boundary conditions

For a high-order flow solver, the reconstruction requires high-order accurate boundary conditions. Here the second-order reconstruction is used to obtain the unknown variables at boundaries. For convenience, the ghost cell concept is adopted. For example, the cell labeled as '−1' corresponds to the 1st cell inside the boundary. If the value of a variable at the boundary W_b is known (Dirichlet problem), its slope can be obtained through Taylor expansion,

$$W'_b = (-6W_b + 7\overline{W}_1 - \overline{W}_2)/2h. \tag{17}$$

Then the value for the ghost cell can be computed as

$$\overline{W}_{-1} = \overline{W}_1 - hW'_b, \quad \overline{W}_{-2} = \overline{W}_2 - 3hW'_b. \tag{18}$$

Another boundary value problem is that the slope W'_b is known (Neumann problem), then the ghost cell values can be directly calculated by the above formula. For viscous flow simulation, the wall boundary conditions can be set up through the combination of the above two types. For example, the non-slip adiabatic condition can be achieved using the first type of boundary condition for velocities and the second type for temperature and density. Higher order accurate boundary conditions can be constructed similarly with more ghost cells.

3. Analysis of high-order BGK (HBGK) scheme

In order to validate Eq. (15) as a correct Navier–Stokes flux function, let us consider the following limiting case. Eq. (15) gives explicitly the time-dependent gas distribution function f at the cell interface under discontinuous initial condition. In a well resolved flow region, such as the flow inside a resolved boundary layer, the reconstructed conservative variable is smooth and continuous. In such a case, the distribution function f_0 has $g^l = g^r$, $a^l = a^r$, $A^l = A^r$, $C^l = C^r$, and $b^l = b^r$. Consequently, Eq. (14) gives $g_0 = g^l = g^r$, and thus $a = a^l = a^r$, $b = b^l = b^r$. Therefore, in the continuous case the gas distribution function f at a cell interface becomes

$$f_{NS} = g_0\left[1-\tau(ua+A)+tA-\tau t(aA+C)u+\left(-\tau t+\frac{1}{2}t^2\right)(A^2+B')\right], \tag{19}$$

which exactly corresponds to a high-order Navier–Stokes gas distribution function in the smooth flow situation. If we compare the above equation with the BGK-Burnett solution [28,18],

$$f_{Burnett} = g_0\left[1-\tau(ua+A)+tA+(2\tau^2-\tau t)(C+aA)u+\left(\tau^2-\tau t+\frac{1}{2}t^2\right)(A^2+B')+\tau^2(a^2+b)u^2+(\tau^2-\tau t)B''\right], \tag{20}$$

the Burnett solutions include more terms, such as those which are proportional to τ^2,

$$g_0(2\tau^2(C+aA)u+\tau^2(A^2+B')+\tau^2(a^2+b)u^2+(\tau^2-\tau t)B''), \tag{21}$$

where B'' is obtained through the condition

$$\langle B'' + B' + A^2 + 2(C + aA)u + (a^2 + b)u^2 \rangle = 0.$$

So, it is interesting to observe that some terms in the Burnett expansion (20) are actually high-order Navier–Stokes terms due to the high-order spatial derivatives. In the gas-kinetic approach, the second-order or higher-order spatial derivatives of flow variables can be used in the gas distribution function, subsequently effect the flux. The additional terms in (21) contained in the Burnett expansion contribute to the instability associated with the Burnett equations at high Mach number case. These terms related to high-order NS solutions do not contribute to the intrinsic instability of the Burnett solution for high frequency waves.

The piece-wise discontinuous initial data is solely due to the numerical requirement as the cell resolution is not enough to resolve the physical flow structure. The NS equations have intrinsic difficulties to cope with the discontinuities because of its continuous assumption for the flow variables in its modeling. Physically, the smoothness of flow variables can be achieved in a time scale much larger than the particle collision time. So, it is invalid for the Navier–Stokes equations in a time scale of particle collision time τ or less after initial breaking down of the discontinuity in the gas evolution process. However, the gas-kinetic equation is valid in all time $t \geqslant 0$, and the solution from the initial breakdown of the discontinuity can be obtained from the BGK model. The kinetic flux function covers the particle free transport ($0 < t < \tau$), the transition regime ($\tau \approx t$), and the hydrodynamic regime ($\tau \ll t$). The difficulties associated with the NS equations are due to the underlying physics of the governing equations, which is a modeling only on the time scale $t \gg \tau$. It is also interesting to observe that in the continuous case for the high-order Navier–Stokes solution, there are no terms being proportional to τ^2, which corresponding viscosity coefficient square. However, under the general discontinuous condition, Eq. (15) clearly shows the terms related to τ^2. This effect is also due to the initial discontinuity and the nonlinearity in the particle relaxation process. In summary, for polynomial distribution functions which are discontinuous at the origin, the Navier–Stokes formulation has no enough physical mechanism to handle the discontinuities.

In this paper, we only present the directional splitting high-order kinetic flux function. However, this scheme can be naturally extended to 2D and 3D cases by developing a high-order multidimensional method using the methodology presented earlier [29,11]. For example, based on the piece-wise polynomial in 3D case on the left and right hand sides of a cell interface,

$$\begin{aligned} W(x,y,z,0) = W_0 + (\partial W/\partial x)x + (\partial W/\partial y)y + (\partial W/\partial z)z + \frac{1}{2}\left((\partial^2 W/\partial x^2)x^2 + (\partial^2 W/\partial y^2)y^2 + (\partial^2 W/\partial z^2)z^2\right) \\ + \left((\partial^2 W/\partial x\partial y)xy + (\partial^2 W/\partial y\partial z)yz + (\partial^2 W/\partial z\partial x)zx\right) + \cdots, \end{aligned} \tag{22}$$

a corresponding non-equilibrium high-order Navier–Stokes gas distribution function f_0 can be constructed. With the expansion of the equilibrium state g, the time evolution f can be obtained based on the integral solution of the BGK model. The scheme is multidimensional because all gradients normal and tangential to a cell surface will participate in the gas evolution process.

In the continuum limit as the flow structure is well-resolved by the cell size, the discontinuities disappear at the cell interface. The above kinetic formulation with the explicit account of particle transport (or upwinding in CFD terminology) will go back to the traditional Chapman–Enskog expansion for the continuum flow (corresponding to central-difference method in CFD community). Therefore, the multidimensional gas-kinetic scheme is a unification of upwinding and central-difference schemes. So, it is not surprising that a high-order gas-kinetic scheme can be developed for the Navier–Stokes solutions under the piece-wise discontinuous initial data where the solutions have both hyperbolic (upwinding) and parabolic (central difference) nature.

4. Numerical experiments

Eight test cases are presented to validate the high-order BGK (HBGK) method for both resolved Navier–Stokes and unresolved discontinuous solutions. The test cases include highly dissipative Navier–Stokes shock structure, the viscous and heat conducting Couette flow, and the laminar boundary layer. In order to illustrate the performance of the new scheme, the results from the second-order BGK-NS method will also be included in certain cases. Unless otherwise stated, in all numerical examples, a specific heat ratio $\gamma = 1.4$ and unity Prandtl number are adopted and the collision time is given by

$$\tau = \tau_m + \tau_a, \tag{23}$$

where the molecular viscosity is calculated by $\tau_m = \mu/p$ for viscous flow and $\tau_m = 0.01\Delta t$ for inviscid case. The second part in the collision time accounts for the artificial numerical viscosity and is chosen to be $\tau_a = 0.1\frac{|p^l - p^r|}{|p^l + p^r|}\Delta t$. The computational time step Δt is determined by

$$\Delta t = \frac{C_{\Delta t}\Delta x}{|U| + a + 2\nu/\Delta x} \tag{24}$$

with the CFL number $C_{\Delta t} = 0.3$ or the value specifically given in the test case. The kinetic viscosity coefficient ν in the above formula is set to zero for inviscid flow. For simplicity, the uniform mesh is used and the reconstruction is based on the third-order polynomial for the advection of density perturbation problem and the shock structure problem. For other cases, the second-order PFGM limiter [30] ($p = 2$) is used mostly for the direct reconstruction of conservative variables. Pressure is checked to identify the trouble cells. Since we are emphasizing the construction of the Navier–Stokes flux function from a high-order polynomials in this paper, we do not intend to use different reconstruction schemes to improve the performance of individual test case.

Case (1): Advection of density perturbation.

This case is calculated to evaluate the accuracy of the present scheme for inviscid smooth flow [20]. The initial condition is set to be $\rho(x) = 1 + 0.2\sin(\pi x)$, $U(x) = 1$ and $p(x) = 1$. The computational domain is chosen as $[-1,1]$ divided by N uniform cells. The periodic boundary condition is adopted and thus the analytic solution is $\rho(x,t) = 1 + 0.2\sin(\pi(x - t))$, $U(x,t) = 1$ and $p(x,t) = 1$. For this inviscid flow, in order to reduce the effect from physical viscosity, here we set the particle collision time as $\tau = (100N)^{-2}\Delta t$.

The computed errors of the density at $t = 2$ is shown in Fig. 2. For this simple case, a fourth-order accuracy can be achieved by the HBGK scheme.

Case (2): Navier–Stokes shock structure.

The performance of the HBGK scheme is tested for the highly dissipative shock structure. The initial condition is set as a stationary shock with inflow Mach number $M = 1.1$, $\rho_1 = 1$, $U_1 = 1$ and $\gamma = 5/3$. The computational domain is chosen as $[-0.025,0.025]$ according to the constant viscosity $\mu = 2.5 \times 10^{-4}$. To fix the location of the shock, based on the analytic

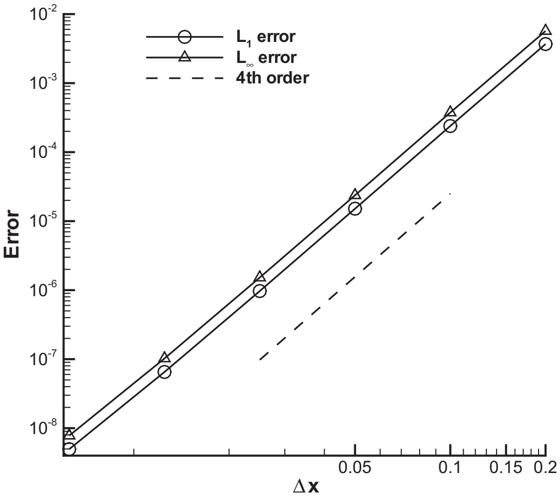

Fig. 2. Error in density vs. cell size for the linear advection of density perturbation.

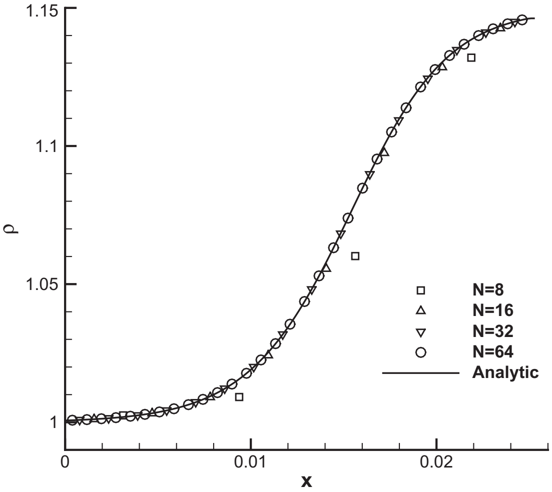

Fig. 3. Density distribution inside a stationary shock layer from HBGK scheme.

solution the Dirichlet condition is adopted at the downstream boundary. For example, the velocity is set, $U = U_2 + 0.02(U_1 - U_2)$ at $x = 0.025$, where U_2 is post-shock velocity computed from Rankine–Hugoniot condition. Other unknowns are calculated through interpolation. The analytic solution is obtained by solving the ordinary differential equations [27].

Fig. 3 shows the computed density distribution with different mesh points. Good mesh convergence is achieved and the NS shock structure can be satisfactorily captured even with only three grid points inside the shock layer ($N = 8$). The deviation from the analytic solution is shown in Fig. 4, where the error norm is calculated with mesh points inside the shock layer ($0 \leqslant x \leqslant 0.025$). Third-order accuracy of the present scheme is confirmed.

Case (3): Blast wave.

The blast wave problem, originally proposed by Woodward and Colella [26], is simulated to evaluate the performance of the present HBGK scheme for flow with strong discontinuities. In this case, the density and pressure are both checked to identify the trouble cells. The computational domain is [0, 1] with reflecting boundary condition on both sides. The initial flow field is stationary with unity density. The pressure is 1000 for $0 \leqslant x < 0.1$, 100 for $0.9 \leqslant x \leqslant 1$, and 0.01 between them.

Figs. 5 and 6 show the computed density and pressure distributions at $t = 0.038$ with mesh number $N = 400$, which are compared with the reference solutions obtained by the BGK-NS scheme with mesh points $N = 400$ and $N = 10,000$, respectively, where van Leer slope limiter is used in the second-order method. The figures show that the strong shock and contact discontinuities, particularly for the local extreme values, are better resolved by the HBGK method. However, in comparison

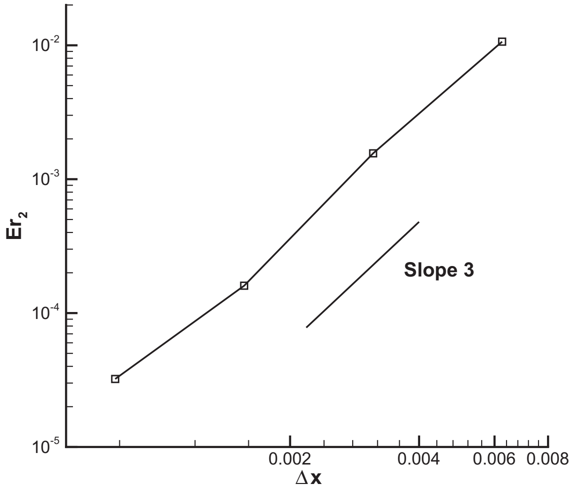

Fig. 4. Variation of error in L2-norm with cell size from the HBGK scheme for shock structure test.

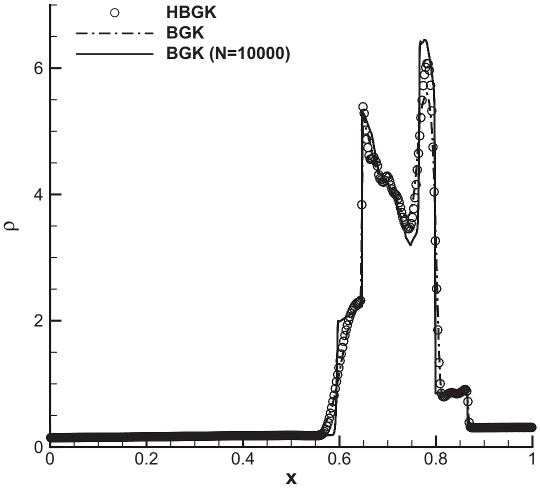

Fig. 5. Density distribution for the Woodward and Colella problem from the current HBGK scheme with 400 points. The reference solutions are obtained from second-order BGK-NS method with 400 and 10,000 points.

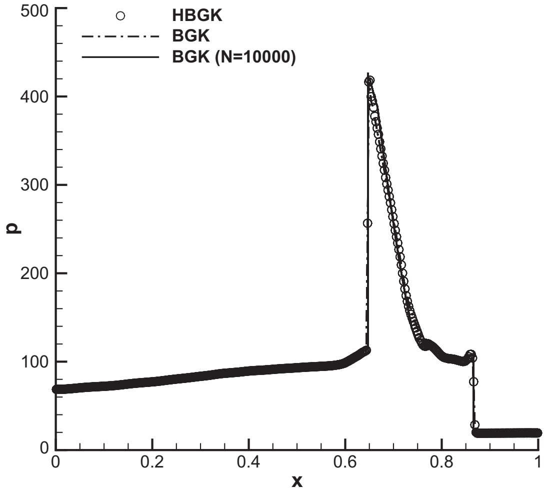

Fig. 6. Pressure profiles for the Woodward and Colella problem.

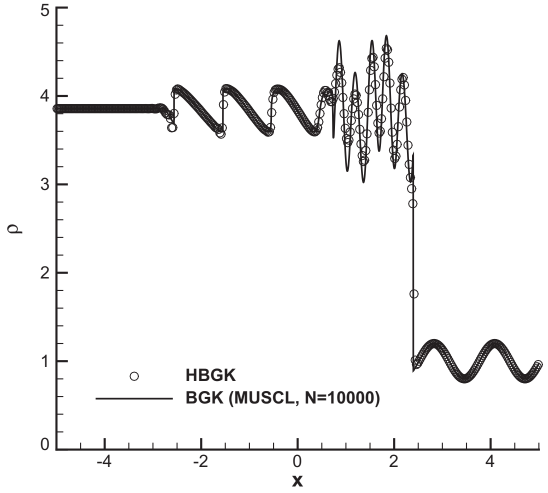

Fig. 7. Density distributions for shock acoustic-wave interaction from HBGK scheme.

with some other high-order schemes in the literature, the computed left-most contact discontinuity from the current scheme looks more diffusive. This may come from the different initial reconstruction used. Here, we directly use the conservative variables in the reconstruction and a simple reconstruction scheme. Also, the HBGK method is developed for viscous flow computation, without special treatment at contact discontinuity, the theoretically NS solution presents a dissipative and smearing contact discontinuity.

Case (4): Shu–Osher shock acoustic-wave interaction.

This problem is the interaction of a moving shock with smooth density fluctuations. The computational domain is $[-5,5]$ and the flow field is initialized as

$$(\rho, U, p) = \begin{cases} (3.857134, 2.629369, 10.33333), & x < -4, \\ (1 + 0.2\sin(5x), 0, 1), & x \geqslant -4. \end{cases} \tag{25}$$

The computed density profiles with mesh points $N = 400$ at time $t = 1.8$ is shown in Fig. 7, which is compared with the reference solution. With the simple second-order PFGM limiter [30], both of the sharp shock discontinuity and acoustic oscillation are well captured. A close-up view of the acoustic region is shown in Fig. 8. It should be noted that the limiter applied in the reconstruction plays an important role for the performance in this test case. If we want to further improve the result, a

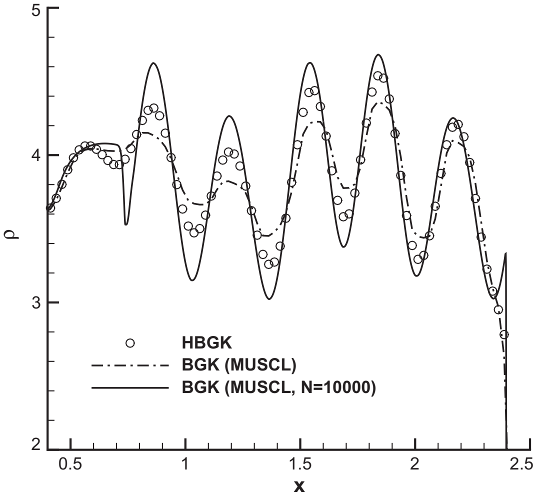

Fig. 8. Detailed density distributions calculated by HBGK and second-order BGK-NS scheme with MUSCL limiter.

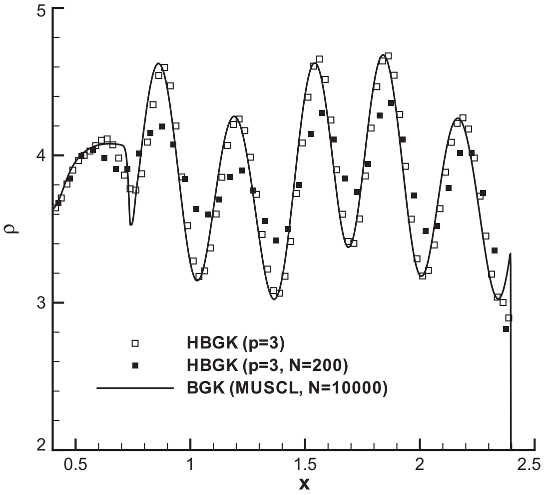

Fig. 9. Detailed density distributions calculated by HBGK with third-order reconstruction.

high-order reconstruction may be a good choice. As shown in Fig. 9, with the help of the third-order PFGM limter ($p = 3$), the local extreme is evidently better resolved with the present HBGK scheme. Even with only half number of cells ($N = 200$) the present HBGK scheme can yield better results than the original second-order BGK-NS method.

Case (5): Couette flow with a temperature gradient.

The Couette flow is a typical test governed by the compressible NS equations, which has an analytical solution. The flow is one-dimensional but with two velocity components.

The left wall is fixed and the right one is moving at a speed 1 in the vertical direction. The temperatures at the left and right are given by T_0 and T_1. Under the assumption of constant viscosity $\mu = 5 \times 10^{-3}$ and heat conduction coefficients, a steady analytic temperature distribution can be deduced,

$$\frac{T-T_0}{T_1-T_0}=\frac{x}{H}+\frac{\mathrm{PrEc}}{2}\frac{x}{H}\left(1-\frac{x}{H}\right), \tag{26}$$

where $H = 1$ is the height of the channel, Pr is the Prandtl number and Ec is the Eckert number $\mathrm{Ec} = U^2/C_p(T_1 - T_0)$. In the present study, $\mathrm{Ec} = 20$ and a Mach number $M = 0.1$ are considered. The CFL number is set to be 0.6.

Fig. 10 shows the computed temperature distributions with different mesh points. Good mesh convergence solution is achieved and the temperature profile is well captured even with only five mesh points by the current HBGK method. This

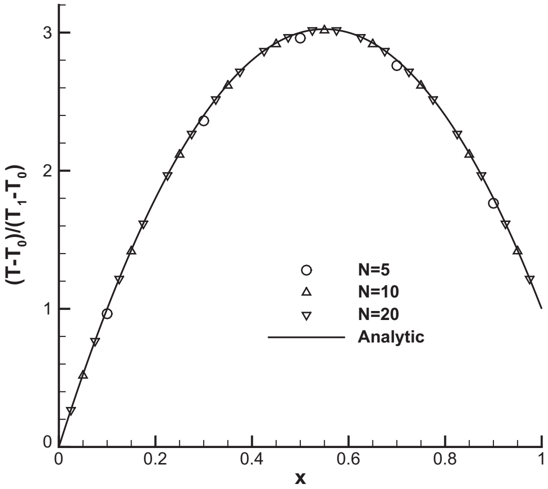

Fig. 10. Temperature ratio profiles in the Couette flow. The solid line labeled by 'analytic' represents the solution given by Eq. (26). Symbols are computed by HBGK scheme with different mesh points.

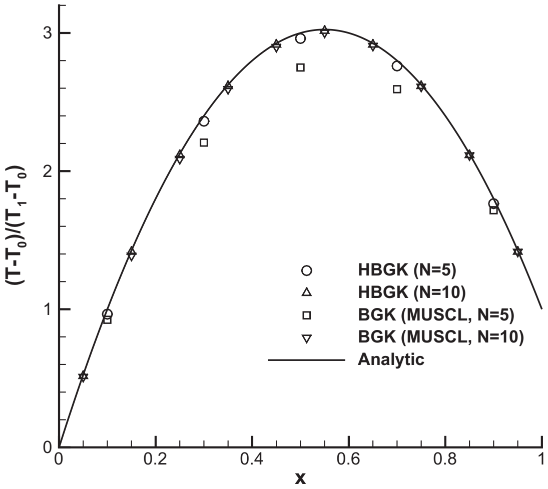

Fig. 11. Comparison of temperature profiles in the Couette flow using HBGK and second-order BGK-NS (MUSCL) with different mesh points.

test case shows that the heat flux can be accurately predicted by HBGK scheme. Furthermore the HBGK works obviously better than the BGK-NS method (see Fig. 11), especially when using less mesh points.

Case (6): Flow near an oscillating plate.

This test case is a low-speed flow near a vertically oscillating flat plate with infinite length. The flow is also dominated by the viscous shear, and the analytical solution can be derived from NS equation as,

$$V(x,t) = V_0 e^{-kx}\cos(\omega t - kx), \tag{27}$$

under the incompressible assumption and the boundary condition, $V(0,t) = V_0\cos\omega t$, and $V(\infty,t) = 0$. Here $k = \sqrt{\omega/2\nu}$ is the wave number and ν is the kinetic viscosity coefficient. In the present study, we set the constants as, $V_0 = 1$, $\nu = 0.01$ and $\omega = 8\pi^2\nu$. Thus the wave length for the damping velocity is $\lambda_x = 2\pi/k = 1$. The computational domain is chosen as [0,3] divided by N uniform cells. The initial flow field is stationary with unity density and pressure $1/\gamma M^2$ with $\gamma = 5/3$ and Mach number $M = V_0/a = 0.1$. The non-slip adiabatic boundary condition at the plate is adopted. At the right boundary, the conservative variables are given based on the analytic solution. The CFL number is set to be 0.6.

Fig. 12 shows the computed velocity distributions at time $t = 22.4$ and 24 with different mesh points. Good mesh convergence is achieved and the velocity profile can be satisfactorily captured even with only several grid points by the current HBGK method.

Case (7): Laminar boundary layer.

This is a low-speed boundary layer test over a flat plate with length $L = 100$. The Mach number of the free-stream is 0.15 and the Reynolds number is $Re = U_\infty L/\nu = 10^5$. As shown in Fig. 13, a total non-uniform 120×30 mesh points are adopted, where 40×30 cells are located ahead of the plate ($x < 0$). The minimal cell sizes are $\Delta x_m = 0.1$ and $\Delta y_m = 0.07$, respectively.

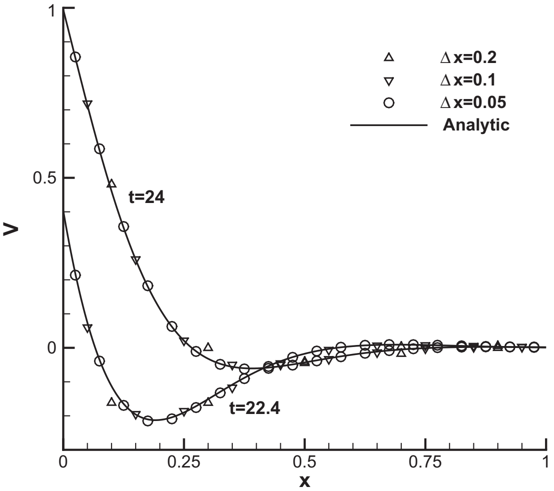

Fig. 12. Velocity profiles for flow near an oscillating plate. The solid line labeled by 'analytic' represents the solution given by Eq. (27). Symbols are computed by HBGK scheme with different mesh points.

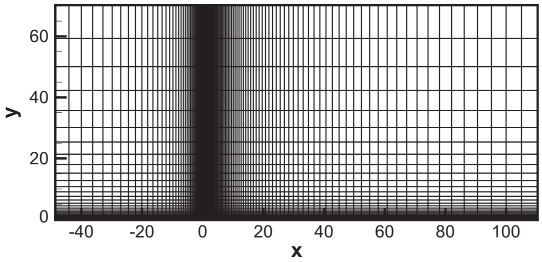

Fig. 13. Computational mesh for flat plate boundary layer.

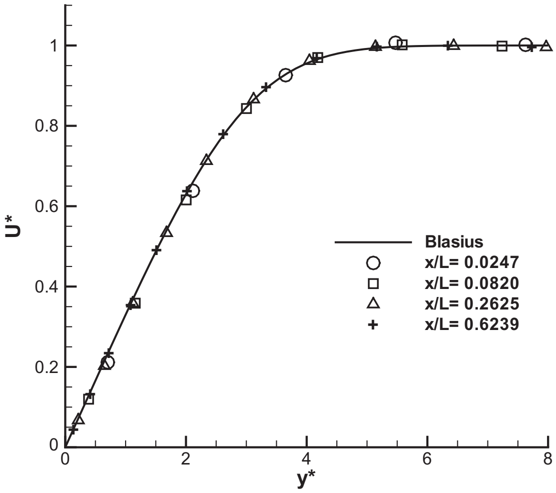

Fig. 14. Streamwise velocity profiles at different locations of a laminar boundary layer.

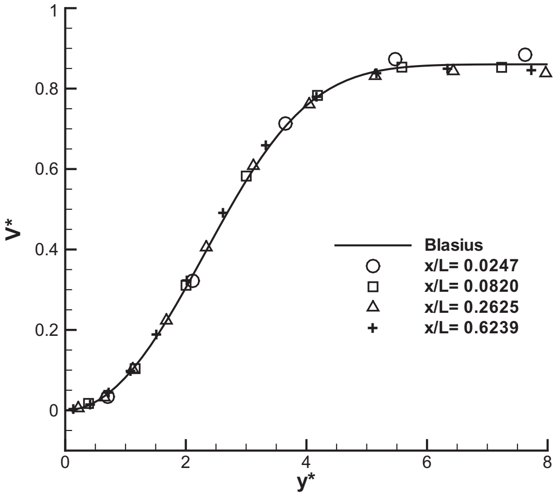

Fig. 15. Transverse velocity profiles at different locations of a laminar boundary layer.

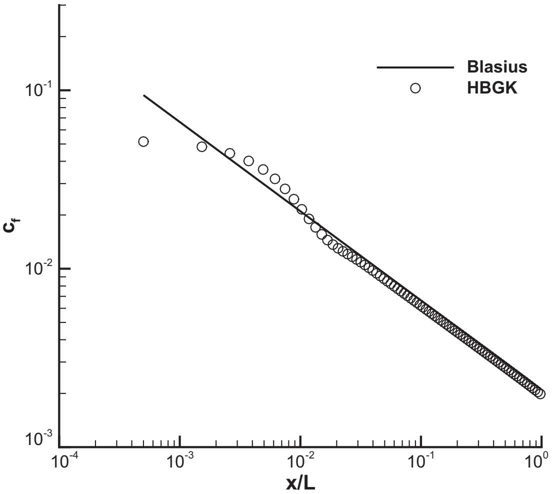

Fig. 16. Skin friction coefficient along the flat plate.

The non-slip adiabatic boundary condition at the plate is used and a symmetry condition is imposed at the bottom boundary before the flat plate. The non-reflecting boundary condition based on the Riemann invariant is adopted for the other boundaries. The CFL number is set to be 0.6.

Figs. 14 and 15 show the calculated velocity, where the non-dimensional variables are defined as $U^* = U/U_\infty$, $V^* = V/\sqrt{\nu U_\infty/x}$ and $y^* = y/\sqrt{\nu x/U_\infty}$. These results clearly show that both streamwise and transverse velocity components can be accurately predicted by HBGK scheme, even with as less as four mesh points in the viscous layer. The computed skin friction coefficient agrees well with the theoretical solution as well (see Fig. 16). These solutions show the good performance of the HBGK scheme for NS solution.

Case (8): Double Mach reflection.

This is a standard test case for inviscid flow, where an incident shock wave with Mach number *10* is reflected from a wedge located at $x = 1/6$ [26]. The computation domain is set to be $[0,3] \times [0,0.75]$. The computation is done with a uniform mesh with mesh size $\Delta x = \Delta y = 1/480$. An enlarged view of density distributions around the triple point are presented in Fig. 17, where the upper one is from the BGK-NS method (with MUSCL limiter) and the lower one is from the current HBGK scheme ($p = 3$). From these figures, it is shown obviously that the HBGK scheme has less numerical dissipation than the BGK-NS method for the inviscid flow computation.

All above test cases validate the excellent performance of the present HBGK scheme. The HBGK scheme works nicely not only for the flows with discontinuities, but also for the viscosity and heat conduction dominated flow, such as the shock

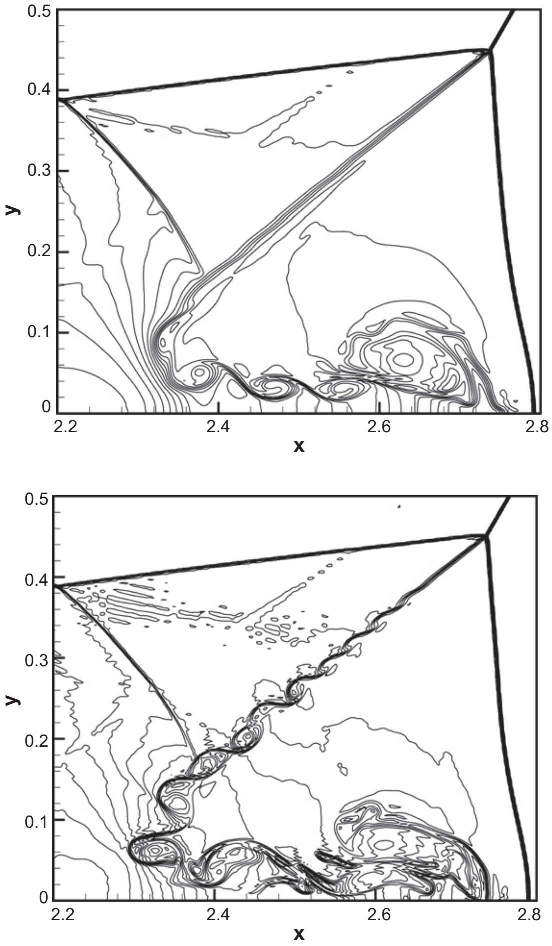

Fig. 17. An enlarged density distributions around the triple point. The upper one is from the BGK-NS method, and the lower one is from the HBGK scheme.

structure and boundary layer. In terms of computational cost, the directional splitting HBGK scheme spends only 50% more computational time than that using BGK-NS method in the 2D double Mach reflection case. Recently, Boger extensively investigated the performance of BGK-NS scheme and their simplifications, especially their computational cost. In his report, the use of the complete BGK-NS method in their elsA code will double the computational cost in comparison with that where Roe flux function is implemented [2].

5. Conclusion

In this paper, we present a high-order gas-kinetic scheme for the Navier–Stokes equations. The scheme provides a time-dependent Navier–Stokes flux function under the generalized piece-wise polynomials for the flow variables with a discontinuity at the origin. In the current high-order scheme, the high-order spatial and temporal derivatives are coupled nonlinearly in the gas evolution process. Due to the incorporation of the whole curves of macroscopic flow variables into the flux evaluation, one obvious advantage of the current scheme is that its solution is not sensitive to the point-wise values at the interface, the so-called initial data for the Riemann problem. A multidimensional gas-kinetic method can be also constructed in 2D and 3D cases. The flux function provided in this paper can be used in many high-order methods, such as DG, SV, and SD, for the compressible Navier–Stokes solutions. The success of the gas-kinetic scheme is due to its the simple particle transport and collision mechanism described by the kinetic equation. For the macroscopic equations, different types, i.e. parabolic and hyperbolic, seek different numerical treatments. The kinetic formulation has the mechanism to capture the particle relaxation process from a discontinuous initial data on a time interval $0 < t < \tau$, and to form a dissipative Navier–Stokes wave structure on a subsequent time scale $t > \tau$. The use of the kinetic flux function is indispensable for the development of reliable high-order CFD methods.

Acknowledgments

This work of Q. Li was supported by National Natural Science Foundation of China (Project No. 10872112). K. Xu was supported by Hong Kong Research Grant Council 621709 and National Natural Science Foundation of China (Project No. 10928205).

References

[1] P.L. Bhatnagar, E.P. Gross, M. Krook, A model for collision processes in gases I: Small amplitude processes in charged and neutral one-component systems, Phys. Rev. 94 (1954) 511–525.

[2] Markus Boger, Implementation of a gas-kinetic BGK solver in the elsA code, Projet de fin d'etudes Tutors at CERFACS, WN/CFD/08/84, 2008.

[3] B. Cockburn, G.E. Karniadakis, C.W. Shu, The development of discontinuous Galerkin methods, in: B. Cockburn, G.E. Karniadakis, C.W. Shu (Eds.), Discontinuous Galerkin Methods, Springer, Berlin, 2000.

[4] X.G. Deng, H.X. Zhang, Developing high-order weighted compact nonlinear schemes, J. Comput. Phys. 165 (2000) 22–44.

[5] S.K. Godunov, A difference scheme for numerical computation of discontinuous solutions of hydrodynamic equations, Math. Sbornik 47 (1959) 271–306.

[6] A. Harten, The artificial compression method for computation of shocks and contact discontinuties: III Self-adjusting hybrid schemes, Math. Comput. 32 (1978) 363–389.

[7] A. Harten, B. Enqguist, S. Osher, S. Chakravarthy, Uniformly high-order essentially non-oscillatory schemes III, J. Comput. Phys. 71 (1987) 231–303.

[8] S. Ii, F. Xiao, High order multi-moment constrained finite volume method. Part I: Basic formulation, J. Comput. Phys. 228 (2009) 3669–3707.

[9] A. Jameson, W. Schmidt, and E. Turkel, Numerical solution of the Euler equations by finite volume methods using Runge–Kutta time stepping schemes, AIAA paper 1981-1259, 1981.

[10] G. Jiang, C.W. Shu, Efficient implementation of weighted ENO schemes, J. Comput. Phys. 126 (1996) 202–228.

[11] Q. Li, S. Fu, On the multidimensional gas-kinetic BGK scheme, J. Comput. Phys. 220 (2006) 532–548.

[12] Q. Li, S. Fu, K. Xu, A compressible Navier–Stokes flow solver with scalar transport, J. Comput. Phys. 204 (2005) 692–714.

[13] Q. Li, S. Fu, K. Xu, Application of BGK scheme with kinetic boundary conditions in hypersonic flow, AIAA J. 43 (2005) 2170–2176.

[14] Q. Li, S. Fu, A high-order accurate gas-kinetic BGK scheme, in: 5th International Conference on Computational Fluid Dynamics, July 7–11, Seoul, Korea, 2008.

[15] Y. Liu, M. Vinokur, Z.J. Wang, Discontinuous spectral difference method for conservation laws on unstructured grids, J. Comput. Phys. 216 (2006) 780–801.

[16] H.W. Liu, K. Xu, A Runge–Kutta discontinuous galerkin method for viscous flow equations, J. Comput. Phys. 224 (2007) 1223–1242.

[17] H. Luo, L. Luo, K. Xu, A discontinuous Galerkin method based on a BGK scheme for the Navier–Stokes equations on arbitrary grids, Adv. Appl. Math. Mech. 1 (2009) 301–318.

[18] T. Ohwada, K. Xu, The kinetic scheme for full Burnett equations, J. Comput. Phys. 201 (2004) 315–332.

[19] M. Oliveria, P. Lu, X. Liu, C. Liu, Universal high order subroutine with new shock detector for shock boundary layer interaction, in: AIAA 2009-1139, 47th AIAA Aerospace Sciences Meeting, 2009.

[20] J. Qiu, C.-W. Shu, Hermite WENO schemes and their application as limiters for Runge–Kutta discontinuous Galerkin method: one-dimensional case, J. Comput. Phys. 193 (2003) 115–135.

[21] W.H. Reed, T.R. Hill, Triangular mesh methods for the neutron transport equation, Technical Report LA-UR-73-479, Los Alamos Scientific Laboratory, 1973.

[22] E. Toro, Riemann Solvers and Numerical Methods for Fluid Dynamics, Springer, 1999.

[23] E. Toro, R.C. Millington, L.A.M. Nejad, Towards very high order Godunov schemes, in: E.F. Toro (Ed.), Godunov Methods: Theory and Applications, Kluwer/Plenum Academic Publishers, 2001, pp. 907–940.

[24] W.G. Vincenti, C.H. Kruger Jr., Introduction to Physical Gas Dynamics, Wiley, New York, 1965.

[25] Z.J. Wang, Spectral (finite) volume method for conservation laws on unstructured grids: basic formulation, J. Comput. Phys. 178 (2002) 210–251.

[26] P. Woodward, P. Colella, Numerical simulations of two-dimensional fluid flow with strong shocks, J. Comput. Phys. 54 (1984) 115–173.

[27] K. Xu, A gas-kinetic BGK scheme for the Navier–Stokes equations, and its connection with artificial dissipation and godunov method, J. Comput. Phys. 171 (2001) 289–335.

[28] K. Xu, Z.H. Li, Microchannel flows in slip flow regime: BGK-Burnett solutions, J. Fluid Mech. 513 (2004) 87–110.

[29] K. Xu, M.L. Mao, L. Tang, A multidimensional gas-kinetic BGK scheme for hypersonic viscous flow, J. Comput. Phys. 203 (2005) 405–421.

[30] M. Yang, Z.J. Wang, A parameter-free generalized moment limiter for high-order methods on unstructured grids, in: AIAA 2009-605, 47th AIAA Aerospace Sciences Meeting Including The New Horizons Forum and Aerospace Exposition, January 5–8, 2009, Orlando, Florida.